polymers

MDPI

Article

Attenuation of the 2.1 THz Band in Heated Microcrystalline Cellulose and Its Reappearance After Cooling

Linquan Cao, Han Wang, Te Ma, Satoru Tsuchikawa and Tetsuya Inagaki *

Graduate School of Bioagricultural Sciences, Nagoya University, Furo-Cho, Chikusa, Nagoya 464-8601, Japan; cao.linquan.m0@s.mail.nagoya-u.ac.jp (L.C.); wh1355@agr.nagoya-u.ac.jp (H.W.); mate@agr.nagoya-u.ac.jp (T.M.); st3842@agr.nagoya-u.ac.jp (S.T.)
* Correspondence: inatetsu@agr.nagoya-u.ac.jp; Tel.: +81-052-789-4157

Abstract

Terahertz time-domain spectroscopy (THz-TDS) probes low-frequency collective vibrations in cellulose, but post-treatment measurements cannot resolve the response of the heated material. Here, three independently prepared microcrystalline cellulose tablets per target temperature were monitored by THz-TDS during 10 min of heating to target stage temperatures of 40–330 °C. The cellulose I-related response near 2.1 THz was evaluated from endpoint spectra and time-resolved fixed-window signals. Tablets treated at eight temperatures were remeasured after cooling and dry equilibration, and the retained state was characterized by X-ray diffraction (XRD) and color analysis. The 2.1 THz response weakened progressively during heating and was no longer resolved at high target temperatures; reliable attenuation midpoints from the 210–330 °C experiments clustered at estimated plate temperatures of 193–236 °C. A reference-only heating control showed only minor variation near 2.1 THz. After cooling, the band remained detectable at every selected temperature, and the independently normalized integrated response showed no corresponding monotonic decline. The post-cooling XRD patterns retained the principal cellulose I_β reflections, whereas pronounced discoloration persisted mainly above approximately 200 °C. In situ THz-TDS revealed changes that could not be reconstructed from the cooled material alone.

Keywords: terahertz time-domain spectroscopy (THz-TDS); microcrystalline cellulose; thermal treatment; phenomenological analysis; X-ray diffraction (XRD); color analysis

1. Introduction

Cellulose is the most abundant natural polysaccharide and a major structural component of lignocellulosic biomass. Its chains are stabilized by intra- and intermolecular hydrogen bonds, producing ordered crystalline domains alongside less ordered regions in cellulose-based materials [1,2]. This crystalline organization affects mechanical properties, dimensional stability, chemical accessibility, enzymatic reactivity, and thermal resistance [3,4]. It also contributes to biomass recalcitrance because tightly packed glucan chains limit molecular accessibility and slow enzymatic deconstruction [5,6]. Monitoring crystallinity-related structural and spectroscopic responses during heating is therefore important for understanding the thermal modification of cellulose and its effects on material properties.

Thermal treatment is widely used in wood and cellulose-based materials to improve dimensional stability, reduce hygroscopicity, and modify physicochemical properties [7]. In wood and related lignocellulosic materials, heat treatment can improve dimensional

Check for updates

Academic Editor: Luis Alves

Received: 20 October 2026
Revised: 16 November 2026
Accepted: 24 November 2026
Published: 25 November 2026

Copyright: © 2026 by the authors. Licensee MDPI, Basel, Switzerland. This article is an open access article distributed under the terms and conditions of the Creative Commons Attribution (CC BY) license.

stability and biological durability, but severe heating can reduce mechanical performance and alter chemical composition, cellulose crystalline structure, degradation behavior, and surface wettability [8,9]. At the molecular and supramolecular levels, heating changes water-associated interactions, hydrogen-bond environments, amorphous regions, polymer-chain integrity, and ordered cellulose domains [10]. Changes in crystallinity are not necessarily monotonic. Wood cellulose can show increased crystallinity under moist or moderate conditions [11,12], whereas longer or more severe treatment can reduce crystalline order [10,11]. These opposing trends point to overlapping processes such as amorphous-region removal, moisture-assisted chain rearrangement, recrystallization, and irreversible degradation [11–13]. Reported glass-transition-like behavior in cellulose spans a broad range and depends strongly on moisture content and measurement method. Modulated differential scanning calorimetry of microcrystalline cellulose (MCC) has identified multiple step transitions in dry material between approximately 132 and 184 °C and showed that water lowers these transition temperatures. Other work on cotton cellulose has distinguished a proposed glass transition at 160–180 °C from dehydration-related changes at 200–220 °C. Reported behavior near 200–220 °C may therefore reflect overlapping mobility-related transitions, water loss, and dehydration rather than a uniquely assignable glass transition [14,15]. Thermogravimetric and crystallographic studies have also shown that thermal stability in lignocellulosic materials depends on cellulose crystallinity and crystallite size [13]. During cellulose heating, visible yellowing, browning, and darkening are often observed. Matsuo et al. showed that these color changes can be described using color coordinates in the International Commission on Illumination (CIE) 1976 $L^*a^*b^*$ (CIELAB) color space and kinetic models; decreasing L^* and increasing a^*, b^*, and ΔE^*_{ab} values track progressive thermal alteration [16]. Color analysis therefore provides a non-destructive record of persistent macroscopic and surface-sensitive thermal alteration.

X-ray diffraction (XRD) is widely used to characterize cellulose polymorphs, lattice spacings, and relative crystalline contributions [3,4]. Although variable-temperature XRD can follow structural changes during heating, XRD measurements in thermal-treatment studies are often performed after cooling; such measurements describe the structure retained after treatment rather than transient changes in the heated material. Calculated crystallinity indices also depend on the analytical method, including the Segal peak-height method, amorphous subtraction, and peak deconvolution [3,4]. These factors motivate the use of complementary measurements that probe different physical responses and can be performed during thermal treatment.

Terahertz time-domain spectroscopy (THz-TDS) offers a complementary route for probing cellulose structure because THz radiation is sensitive to low-frequency collective motions, hydrogen-bonding networks, and lattice phonons. It has been used to quantify MCC crystallinity, distinguish cellulose I allomorphs, and follow the transformation from cellulose I to cellulose II, showing that cellulose crystalline structures produce characteristic absorption features in the low-frequency THz region [17–19]. Combined THz, XRD, and solid-state density functional theory studies further showed that disorder in cellulose hydrogen-bond networks affects THz vibrational spectra, which supports the sensitivity of THz-TDS to changes in cellulose crystal packing [20]. Cellulose I has characteristic THz absorption bands near 2.1 and 3.0 THz: the 2.13 THz peak is associated with cellulose I_β, and the 3.04 THz band is related to cellulose I content [18,19,21]. These reports support the use of cellulose-related THz bands, particularly the 2.1 THz band, as probes of crystallinity-related low-frequency vibrational behavior.

Thermal-treatment studies have also started to apply THz-TDS to cellulose-based materials. In heated cellulose and wood powder, the integrated intensity of the cellulose I 3.04 THz band was compared with XRD-derived crystallinity. The reported results showed

rapid crystallinity loss at 250 °C, a slower decrease at 200 °C, and possible recrystallization during lower-temperature treatment [22]. The same study indicated that THz-TDS and XRD respond to different aspects of structural order. XRD reports Bragg-coherent periodic order, whereas low-frequency THz spectra reflect collective vibrations that are sensitive to interchain organization and thermal state. Thermal disorder or local distortion may therefore alter a THz band without eliminating the Bragg reflections retained after cooling. The two methods consequently provide complementary views of thermally induced changes in cellulose. Because those THz measurements were made after thermal treatment, they do not resolve the evolution of the band during heating or establish whether the heated and cooled states exhibit the same spectral response.

Here, time-resolved THz-TDS follows the cellulose I-related response near 2.1 THz in MCC throughout the temperature ramp and subsequent holding period of a 10 min heating protocol. The same tablets at selected treatment temperatures were remeasured after cooling and dry equilibration, with XRD and color analysis used to characterize the retained state. This comparison links the spectral evolution during heating to the response of the cooled material and tests which changes can be identified only by measurements during active heating.

2. Experimental

2.1. Sample Preparation

MCC (Avicel® PH-101, Sigma-Aldrich, St. Louis, MO, USA) was used as the sample material. For each tablet, 75 mg of MCC was compressed into a 12 mm diameter tablet using a manual hydraulic press (IMC-180C, Imoto Machinery Co., Ltd., Kyoto, Japan). The load was released as soon as the instrument gauge reached 50 MPa, without an additional dwell period. Three tablets were independently prepared for each target temperature, with each tablet subjected to one heating run. The initial thickness of each tablet was measured and recorded using a micrometer (±0.001 mm); the measured thicknesses ranged from 0.44 to 0.46 mm. A thickness decrease of approximately 0.05 mm was observed in paired measurements before and after thermal treatment. After preparation, the tablets were stored in a sealed box continuously purged with dry air until transfer to the THz measurement chamber.

2.2. Sample Measurements

2.2.1. THz-TDS Measurement

The THz transmission spectra were acquired using a Tera Prospector-Kit (NIPPO PRECISION Co., Ltd., Nirasaki, Japan) over a spectral range of approximately 0.1–4.00 THz, with a nominal resolution of 0.02 THz. The exported spectra used for analysis contained 145 frequency points from approximately 0.206 to 3.502 THz, with a point spacing of 0.022888 THz. The THz beam was horizontally polarized and focused onto the sample, producing a spot diameter of approximately 3 mm. For all THz measurements, reference spectra were recorded immediately before and after each sample measurement, and the two reference spectra were averaged before calculation of the absorption coefficient. A separate reference-only measurement was also performed during heating under the same acquisition and chamber conditions to assess possible temperature-dependent changes in the reference signal and chamber background. To reduce the influence of atmospheric water vapor, the optical system was enclosed in an acrylic chamber that was continuously purged with dry air. Before both the initial heating measurements and the post-cooling remeasurements, the tablets were conditioned in the dry-air-purged chamber for at least 24 h to allow equilibration with the chamber atmosphere.

2.2.2. Conditions of Thermal Treatment

Thermal treatment during the THz-TDS measurements was conducted using a transmission-mode heating sample stage (TP-HEA-1, NIPPO PRECISION Co., Ltd., Japan) installed in the Tera Prospector system. After each MCC tablet was mounted, the stage unit was manually evacuated to a pressure below 50 Pa and sealed before measurement. Heating was provided by an electric heater, and the temperature of the metal part in contact with the tablet was monitored using a K-type thermocouple. Therefore, the temperatures reported in this study refer to the monitored stage temperature at the sample-contacting metal part rather than the internal temperature of the tablet. Cooling water was circulated through the stage using a chiller for heat dissipation.

Each tablet was heated only once from an initial temperature of 25 °C to its assigned target temperature. The target temperatures ranged from 40 to 330 °C at 10 °C intervals. The spectrum acquired at 25 °C immediately before heating was defined as A_0. For every target-temperature experiment, THz acquisition began at the onset of heating and continued for 10 min using the same acquisition protocol, yielding 125 time-resolved spectra per run. The heating rate was governed by the stage controller and was not independently adjustable. The target temperature was considered to have been reached when the temperature displayed by the controller stabilized at the set value. The acquired spectra therefore covered both the temperature ramp and the subsequent stabilization or holding period.

2.2.3. Post-Cooling THz Measurement

After thermal treatment, the tablets corresponding to target temperatures of 40, 120, 150, 180, 210, 230, 270, and 330 °C were allowed to cool to room temperature and were stored at 25 °C in a sealed box under a dry-air atmosphere until they were transferred to the measurement chamber for post-cooling THz analysis. Post-cooling THz spectra were acquired using the same instrument, optical configuration, sample-mounting procedure, and dry-air-purged chamber conditions as those used for the initial measurements.

2.2.4. XRD Measurement and Data Analysis

XRD patterns of the tablets were collected in reflection mode with an automated diffractometer (Ultima IV, Rigaku, Tokyo, Japan) using Cu-Kα radiation ($\lambda = 0.15418$ nm) at 40 kV and 40 mA. The thermally treated tablets were measured after cooling over a 2θ range of 5–30°. One unheated tablet from the same preparation batch, pressed and dried under the same conditions, was measured using the same instrument settings. Both datasets were acquired at a scanning speed of 5° min^{-1} and a sampling step of 0.05°.

Each XRD pattern was corrected by subtracting its corresponding empty-holder pattern. No further global baseline correction was applied, and negative intensities resulting from the subtraction were retained. All comparisons and fits used the common 2θ = 10–30° interval because the lower-angle region was affected by background-subtraction artifacts.

For whole-pattern shape comparison, each pattern was normalized by its integrated intensity over 2θ = 10–30°. A low-temperature reference pattern was constructed from measurements of three independently prepared tablets at each target temperature from 40 to 90 °C. Each pattern was rigidly aligned to this reference to reduce small angular offsets associated with specimen positioning. Pearson correlation coefficients were then calculated between each aligned pattern and the reference over $13° \leq 2\theta \leq 26°$.

Peak deconvolution was performed on individual background-corrected patterns within 2θ = 10–30°, without prior area normalization or rigid alignment. A low-temperature reference model was established from the 40–90 °C reference pattern using Gaussian functions for the cellulose I_β $\left(1\bar{1}0\right)$, (110), and (102) reflections and a Voigt function for the dominant (200) reflection. The amorphous component was evaluated from the eighth-order

real Fourier series and coefficients published by Yao et al. [23] (pp. 5572–5573), which describe their ball-milled cellulose reference. The 10–30° segment was normalized to unit area, and its Fourier coefficients were held fixed. In each individual fit, the five component areas were constrained to non-negative values and the components shared a common angular shift. A common width-scaling factor was applied to the three Gaussian components, with a separate factor for the (200) Voigt component. For representative deconvolution plots, the aligned, area-normalized profiles of three tablets were averaged at each selected temperature and refitted using the same constrained model. The crystalline-area fractions and (200) widths were obtained from the individual unnormalized, unaligned patterns.

The apparent crystalline-area fraction was calculated as the summed integrated area of the four crystalline components divided by the combined crystalline and amorphous areas within 10–30°. Results for the thermally treated series are reported as mean ± standard deviation from three independently prepared tablets at each target temperature. The unheated reference was fitted with the same model and is reported as a single value; it was not included in the low-temperature reference or the treatment-series statistics.

Sensitivity to the assumed amorphous profile was examined using nine combinations of independent angular shifts (−0.5°, 0°, and +0.5°) and width scales (0.90, 1.00, and 1.10) about the original profile maximum. A Gaussian matched to the original profile's principal-peak position and half-height width was tested separately. For each profile, the low-temperature reference model and all 90 individual post-cooling patterns were refitted using the original constraints. These predefined perturbations provide a local sensitivity check.

2.3. THz Spectral Processing and Peak Analysis

The refractive index and absorption coefficient were calculated using a fixed nominal tablet thickness of 0.45 mm for both heating and post-cooling measurements. The nominal thickness was expressed as 4.5×10^{-4} m in the phase-based refractive-index calculation with the speed of light in m s^{-1}, and as 0.045 cm when calculating the absorption coefficient in cm^{-1}. Tablet thickness was not monitored during heating, and treatment-induced changes in optical path length were not included in the calculation.

For peak fitting and spectral visualization, each absorption-coefficient spectrum was independently transformed using standard normal variate (SNV) normalization. The mean and sample standard deviation were calculated across the full exported interval of approximately 0.206–3.502 THz (145 points), before selection of the fitting or display interval. The normalized spectrum was then smoothed with a second-order Savitzky–Golay filter using a 21-point window spanning approximately 0.458 THz. Window spans are reported as $(N-1)\Delta f$, where N is the number of points and Δf is the spectral point spacing.

To characterize changes in the complete 2.1 THz band, the endpoint spectrum at each target temperature was obtained by averaging the final six spectra after this preprocessing. It was fitted using a pseudo-Voigt peak model [24], written here in a peak-height parameterization and combined with a linear baseline. Quantitative fitting used the fixed frequency range of 1.72–2.38 THz, without endpoint-to-endpoint baseline subtraction, zero clipping, or additional smoothing. The fitting function was defined as Equation (1):

$$Y(f) = b_0 + b_1(f - f_c) + H\left[(1-\eta)\exp\left(-4\ln 2\left(\frac{f-f_c}{w}\right)^2\right) + \frac{\eta}{1+4\left(\frac{f-f_c}{w}\right)^2}\right]. \quad (1)$$

where f_c is the peak center frequency, w is the full width at half maximum (FWHM), H is the baseline-corrected peak height, η is the Lorentzian mixing fraction in this peak-height

parameterization, and b_0 and b_1 describe the linear baseline. The parameters were determined using bounded nonlinear least-squares fitting. The center frequency was constrained to 1.85 to 2.30 THz, the FWHM to 0.08 to 0.80 THz, the peak height to non-negative values, and the Lorentzian fraction to the interval from 0 to 1.

The peak center frequency, FWHM, peak height, and full fitted peak area were extracted from each spectrum. The full area was derived by analytically integrating the pseudo-Voigt peak term in Equation (1) over the full frequency axis, excluding the linear baseline. The Gaussian and Lorentzian terms contribute area factors of $w\sqrt{\pi}/(2\sqrt{\ln 2})$ and $w\pi/2$, respectively, giving Equation (2):

$$\begin{aligned} A &= \int_{-\infty}^{+\infty} [Y(f) - b_0 - b_1(f - f_c)]\,\mathrm{d}f \\ &= Hw\left[(1-\eta)\frac{\sqrt{\pi}}{2\sqrt{\ln 2}} + \eta\frac{\pi}{2}\right]. \end{aligned} \tag{2}$$

The numerical integral within the fitting range was also calculated as a consistency check. Parameter covariance was estimated from the residual variance and the Jacobian matrix. Two-sided 95% confidence intervals were calculated using Student's t distribution. The uncertainty of the full fitted area was estimated by first-order error propagation, including the covariance terms among H, w, and η. The coefficient of determination and root mean square error were retained as additional goodness-of-fit measures.

Peak identifiability was assessed using both fit stability and signal-to-noise ratio (SNR). The SNR was defined as the fitted peak height divided by the robust standard deviation of the fitting residuals. Residual noise was estimated as 1.4826 times the median absolute deviation, with the ordinary residual standard deviation used when the robust estimate was unavailable. Fits with an SNR of at least 5 were classified as quantitative, those with $3 \leq \mathrm{SNR} < 5$ as borderline, and those with $\mathrm{SNR} < 3$ as not identifiable. In addition, an identifiable fit required successful optimization, a lower 95% confidence limit for the peak height above zero, finite confidence intervals, a valid covariance estimate, and fitted parameters that did not reach their prescribed bounds. A fit failing any of these structural criteria was classified as not identifiable regardless of its nominal SNR.

All fitting results were retained in the output for traceability. However, the center frequency and FWHM obtained from non-identifiable fits were excluded from trend analysis and statistical interpretation. Only quantitative fits were included in the calculation of replicate means, standard deviations, and confidence intervals, whereas borderline fits were reported separately as supporting observations.

The fixed display limits of 1.64795 and 2.58636 THz in Figure 1 were selected with guidance from a second-derivative analysis of an unheated tablet spectrum obtained by averaging 100 scans after tablet preparation and drying. After SNV normalization and the 21-point smoothing described above, the second derivative was calculated using a second-order Savitzky–Golay polynomial with a 41-point window (approximately 0.916 THz), with constant-value padding at both ends. The selection used the nearest local maxima on either side of the second-derivative minimum associated with the 2.1 THz band. These display limits were held fixed across temperatures and measurement sets.

For qualitative visualization of the heating-endpoint and post-cooling spectra, the SNV-normalized, 21-point-smoothed spectra were cropped using the derivative-guided limits of 1.64795–2.58636 THz described above. Applying these limits to the discrete frequency grid retained 40 points spanning approximately 1.67084–2.56348 THz. A linear baseline connecting the first and last retained points was subtracted, and negative values were set to zero. For the heating series, the final six processed spectra were averaged to obtain the endpoint curve; each post-cooling curve was obtained from one independently measured spectrum. An additional second-order, nine-point Savitzky–Golay smoothing step (approximately

0.183 THz) was applied to these plotted curves. These display steps were separate from the quantitative peak-fitting procedure. The plotted SNV spectra compare band visibility and shape; their amplitudes are not absolute absorption coefficients.

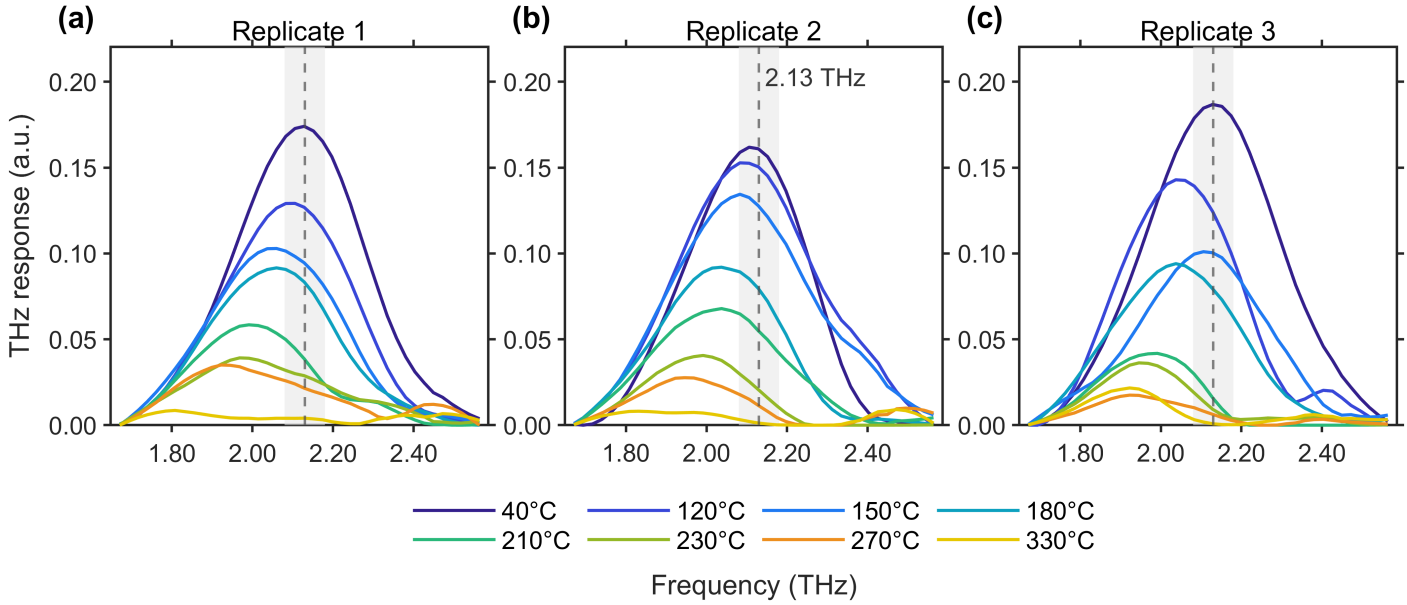


Figure 1. Endpoint terahertz (THz) spectra from three independent measurement sets. Panels (**a**–**c**) correspond to separate sets. For each target temperature, the endpoint spectrum was calculated by averaging the final six time-resolved spectra. The response is expressed in arbitrary units (a.u.). The contributing spectra were independently processed using standard normal variate (SNV) normalization as described in Section 2.3; the plotted curves therefore represent relative spectral prominence rather than absolute absorption coefficients. The shaded region marks the 2.13 ± 0.05 THz integration window used to calculate the fixed-window response A.

To compare the temperature-dependent trends of the heating-endpoint and post-cooling responses without spectrum-wise normalization, an independent integrated-response metric, R_{int}, was calculated from the absorption-coefficient spectra. For each heating run, the final six absorption spectra were first averaged to obtain the endpoint spectrum. No SNV or spectrum-wise maximum normalization was applied. All spectra were smoothed using a second-order Savitzky–Golay filter with a nine-point window spanning approximately 0.183 THz. A linear baseline was fitted using the regions from 1.648 to 1.750 THz and from 2.500 to 2.586 THz and was subtracted from the smoothed spectrum. The signed baseline-corrected response was then integrated from 1.75 to 2.45 THz, without zero clipping. Within each measurement state and independent measurement set, the resulting integrated value was normalized separately to the corresponding value at 40 °C, such that $R_{\mathrm{int}}(T) = I(T)/I(40\,^{\circ}\mathrm{C})$. Mean values and sample standard deviations were calculated from the three independent measurement sets. Because the 40 °C normalization was performed separately for the heating-endpoint and post-cooling series, R_{int} describes temperature-dependent trends within each measurement state rather than an absolute recovery fraction between sessions.

To assess baseline-placement sensitivity, the original four left-side anchor points were shifted toward lower frequencies by zero, one or two measured frequency bins, and the three right-side points by −2 to +2 bins. This gave 15 linear-baseline placements, with a maximum displacement of approximately 0.04578 THz; all anchor points remained outside the 1.75–2.45 THz integration interval. Smoothing and integration settings were held fixed, and each variant was normalized to its own 40 °C integral within each measurement

state and set. The range of replicate means across these settings was used to describe processing sensitivity.

2.4. Phenomenological Analysis of the 2.1 THz Attenuation

For fixed-window integration, the SNV-normalized, 21-point-smoothed spectra were cropped to 1.64795–2.58636 THz, and a straight line joining the first and last retained points was subtracted from each spectrum. The initial spectrum provided A_0; the final six spectra or each consecutive group of six were averaged before negative values were set to zero and the response was integrated. Trapezoidal integration used the five measured frequency points within 2.08–2.18 THz (approximately 2.08282–2.17438 THz), without interpolation to the window boundaries or additional smoothing.

For the time-resolved heating data, the normalized response integrated over the 2.13 ± 0.05 THz window was fitted using a standard logistic function [25], reparameterized with its upper asymptote fixed at 1 to describe attenuation of the cellulose-I-related 2.1 THz response. For the time-resolved analysis, spectra acquired after $t = 0$ were averaged in consecutive non-overlapping groups of six, corresponding to approximately 30 s per grouped observation. The fixed-window response of each grouped spectrum was then divided by A_0, and only complete groups were retained. This frequency window was selected because previous THz studies assigned the 2.13 THz band to cellulose I_β and linked it with crystallinity-sensitive absorption in MCC [18,19,21]. The response was fitted using Equation (3):

$$Y = Y_{\min} + \frac{1 - Y_{\min}}{1 + \exp\left[-k\left(t - t_{1/2}\right)\right]}. \quad (3)$$

where

$Y_{\min}$ is the fitted lower-asymptotic normalized response after attenuation;

k is the signed steepness parameter, with negative values representing decay under the sign convention used in Equation (3);

$t_{1/2}$ is the apparent midpoint time at which the fitted response lies halfway between the fixed upper asymptote of 1 and the fitted lower asymptote $Y_{\min}$, i.e., $Y = (1 + Y_{\min})/2$.

The time-resolved A/A_0 metric is distinct from the integrated-response metric R_{int} defined above. A/A_0 uses the preheating spectrum of each heating run as its reference and integrates the narrow 2.13 ± 0.05 THz window, whereas R_{int} integrates the broader 1.75–2.45 THz range and is normalized separately to the corresponding 40 °C value within each measurement state.

The sensitivity to peak displacement was assessed using quantitative endpoint fits between 40 and 100 °C. Within each measurement set, the 40 °C peak height, FWHM, and mixing fraction were held fixed while only the center was moved to its fitted value at each target temperature. The peak component was integrated analytically over 2.08–2.18 THz and normalized to its 40 °C integral. The calculation was also repeated on the measured frequency grid with endpoint-to-endpoint baseline subtraction and zero clipping. As a direct check on A/A_0 at 100 °C, the endpoint integration nodes were shifted by the fitted center displacement relative to that run's preheating spectrum; endpoint values at the shifted nodes were linearly interpolated, with A_0 unchanged. This check used only runs with quantitative preheating and endpoint fits.

With $t = 0$ assigned to the spectrum acquired before heating, the fitting covered both the temperature ramp and subsequent stabilization. The fitted parameters characterize the attenuation under the applied ramp-and-hold protocol.

To relate the fitted attenuation profiles to the heating program, elapsed time was converted to estimated plate temperature using a common plate-heating calibration measured

in this study from 24 to 330 °C over 120 s. An endpoint-constrained cubic polynomial was fitted to these measured data to establish the empirical calibration relation in Equation (4):

$$T_{\mathrm{cal}}(t) = 8.34233 \times 10^{-5} t^3 - 0.0295544 t^2 + 4.89523 t + 24 \quad (4)$$

where t is expressed in seconds and T_{cal} in degrees Celsius. The fit gave $R^2 = 0.99897$. For each experiment, we defined the piecewise mapping in Equation (5) from this calibration. It assumes that the same calibrated ramp applies to all target settings and that the plate remains at the target temperature once that temperature is reached:

$$T_{\mathrm{plate,est}}(t; T_{\mathrm{target}}) = \begin{cases} \min\left\{T_{\mathrm{cal}}(t), T_{\mathrm{target}}\right\}, & 0 \le t \le 120\,\mathrm{s}, \\ T_{\mathrm{target}}, & t > 120\,\mathrm{s}. \end{cases} \quad (5)$$

Each grouped response was assigned the estimated plate temperature corresponding to the temporal midpoint of its 30 s acquisition interval.

A logistic fit was considered reliable for temperature-aligned interpretation when all fitted parameters were finite, $0 \le Y_{\mathrm{min}} \le 1$, $k < 0$, $t_{1/2}$ lay within the observed fitting interval, and $R^2 \ge 0.70$. This calibration represents the plate temperature and does not account for run-specific overshoot, thermal contact resistance, or temperature lag within the tablet.

2.5. Tablet Color Analysis

Tablet color was evaluated from red-green-blue (RGB) images acquired after thermal treatment using an EPSON GT-S650 scanner (Seiko Epson Corporation, Suwa, Japan) at 600 dots per inch (dpi). A blank-background image and an image of an unheated MCC tablet provided fixed background and unheated-tablet CIELAB references, respectively. The same reference images were used for all three measurement sets. The background reference was calculated from the central 50% × 50% rectangular region of the blank image. For the unheated reference, mean L^*, a^*, and b^* values were calculated within a circle having a radius equal to 60% of the detected tablet radius.

Within each measurement set, groups of three tablets corresponding to consecutive target temperatures were scanned together. The three independent tablets at each temperature were represented by one tablet from each set. Images were analyzed using MATLAB R2024b. The central 75% of each three-tablet image was selected to limit the circle-search region. Contrast-limited adaptive histogram equalization was applied to the grayscale image for tablet detection, followed by circle detection using dark- and bright-object polarity settings. When automatic detection did not identify three tablets reliably, the tablet centers were selected manually. Color values were extracted from the original RGB image within the central 60% of each tablet radius.

RGB values were converted to CIELAB using the MATLAB function rgb2lab with the default standard RGB (sRGB) input space and D65 reference white, and the mean L^*, a^*, and b^* values were calculated over the selected pixels. No calibration against a color standard was performed for the scanner-based analysis. The color coordinates and color differences were therefore treated as comparative image-derived values under these scanning conditions. The overall color difference relative to the fixed unheated-tablet reference was calculated using the standard CIELAB Euclidean color-difference formula [26], as shown in Equation (6):

$$\Delta E^*_{\mathrm{ab}} = \sqrt{\left(L^* - L^*_0\right)^2 + \left(a^* - a^*_0\right)^2 + \left(b^* - b^*_0\right)^2}. \quad (6)$$

where L^*_0, a^*_0, and b^*_0 are the mean CIELAB values of the unheated reference tablet. The temperature-dependent L^*, a^*, b^*, and ΔE^*_{ab} values are reported as mean ± standard deviation from three independently prepared tablets. Color swatches were reconstructed

from the temperature-wise mean CIELAB coordinates. Representative scans were displayed alongside the swatches: the 40 °C scan was from measurement set 3, the 120 °C scan was from measurement set 2, and the remaining scans were from measurement set 1. The scans were cropped to show complete tablets and surrounding background at a common scale, without additional brightness, contrast, or color adjustments.

3. Results and Discussion

3.1. Temperature-Dependent THz Spectral Evolution

The MCC tablets exhibited a THz absorption band near 2.1 THz, consistent with the characteristic response assigned to cellulose I. Figure 1 presents representative endpoint spectra at selected target temperatures from three independent measurement sets. In all three sets, the band was prominent at lower target temperatures and became progressively less prominent as the target temperature increased. Although the detailed band shape varied among the independent measurements, only a weak remaining signal was observed within the displayed frequency range at 230 °C and above. These spectra therefore show a reproducible attenuation of the cellulose-I-related low-frequency vibrational response with increasing target temperature. Although atmospheric water vapor has a reported rotational absorption line at 2.164 THz within the 2.13 ± 0.05 THz window [27], the reference-only heating measurement showed only minor variation around 2.1 THz compared with the pronounced attenuation observed for the MCC tablets. This comparison identifies the sample as the dominant source of the temperature-dependent change.

The higher-frequency region near 3.04 THz showed substantial point-to-point variations and inconsistent band shapes across the heating series, which limited reliable quantification of its peak height and position. The analysis therefore focuses on the 2.1 THz response.

Quantitative pseudo-Voigt fitting was used to examine changes in the center frequency, FWHM, peak height, and full fitted area of the 2.1 THz band (Figure 2). Of the 90 endpoint spectra, 30 met all convergence, uncertainty, boundary, and SNR criteria for quantitative interpretation. Reliable fits were obtained most consistently between 40 and 100 °C. Within this range, the mean fitted center frequency decreased from 2.128 THz at 40 °C to 2.096 THz at 100 °C, while the fitted peak height and full fitted area also decreased overall. In contrast, the FWHM did not show a consistent change across the three measurement sets. Above 110 °C, valid fits became increasingly sparse, and none of the spectra measured at 230 °C or above yielded an identifiable peak center or linewidth. The loss of identifiability at higher temperatures reflects the attenuation of the 2.1 THz feature and prevents reliable interpretation of peak position or FWHM in this region. The peak-shape analysis therefore demonstrates attenuation and a low-temperature shift of the cellulose-I-related collective response. The FWHM showed no reproducible temperature dependence.

Figure 3 presents the complete endpoint spectral series as frequency–temperature maps using a common color scale for all three measurement sets.

In all three measurement sets, the high-response region was concentrated near 2.0 to 2.2 THz at lower target temperatures. As the target temperature increased, this region progressively weakened and contracted in both frequency and temperature extent. At higher temperatures, only a weak and nonuniform response remained around 2.13 THz. The temperature range over which the high-response region persisted differed among the measurement sets, indicating variability in the onset and progression of attenuation, although the overall loss of the 2.1 THz feature was reproduced. These endpoint maps describe the extent of attenuation as a function of target temperature, rather than its temporal rate.

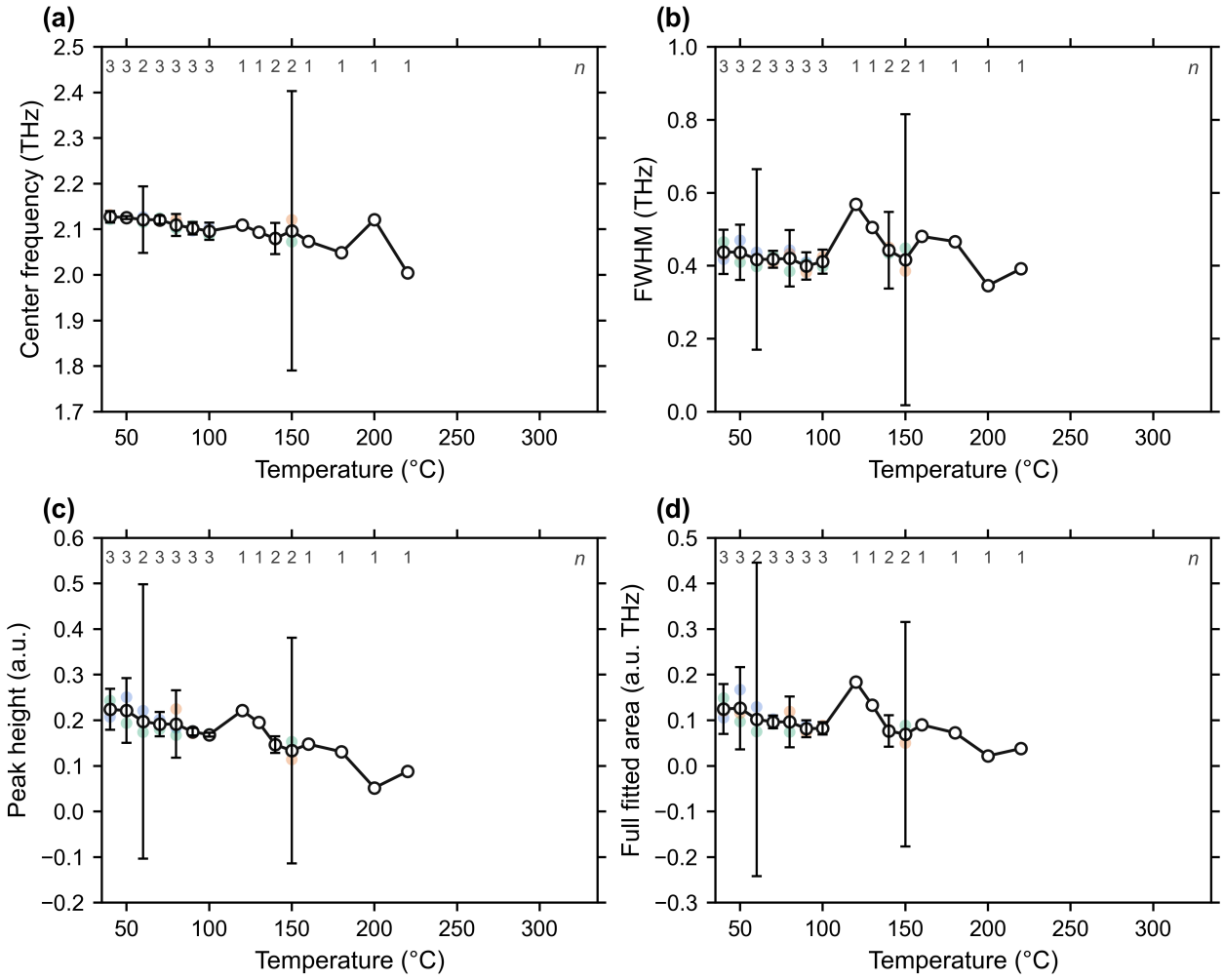


Figure 2. Temperature dependence of the fitted parameters of the 2.1 THz band. Mean values of (**a**) center frequency, (**b**) full width at half maximum (FWHM), (**c**) peak height, and (**d**) full fitted area obtained from endpoint spectra classified as quantitative. Blue, green, and orange filled symbols show individual quantitative fits from measurement sets 1, 2, and 3, respectively. Black open circles connected by black lines show the means; the connecting lines are visual guides. Error bars indicate two-sided 95% confidence intervals for the mean when at least two quantitative fits were available. Numbers along the top of each panel indicate the number of quantitative fits contributing to the plotted mean at the corresponding temperature. Temperatures without an identifiable quantitative fit are not plotted.

To summarize endpoint attenuation over the full temperature range without requiring an identifiable peak fit, the response within the fixed 2.13 ± 0.05 THz window was expressed as A/A_0 (Figure 4). Unlike the fitted center frequency and FWHM, this fixed-window metric could still be calculated after the 2.1 THz band became too weak for reliable peak-shape fitting. In this region, the metric represents the remaining baseline-corrected signal within the selected frequency window, rather than the area of a resolved 2.1 THz peak.

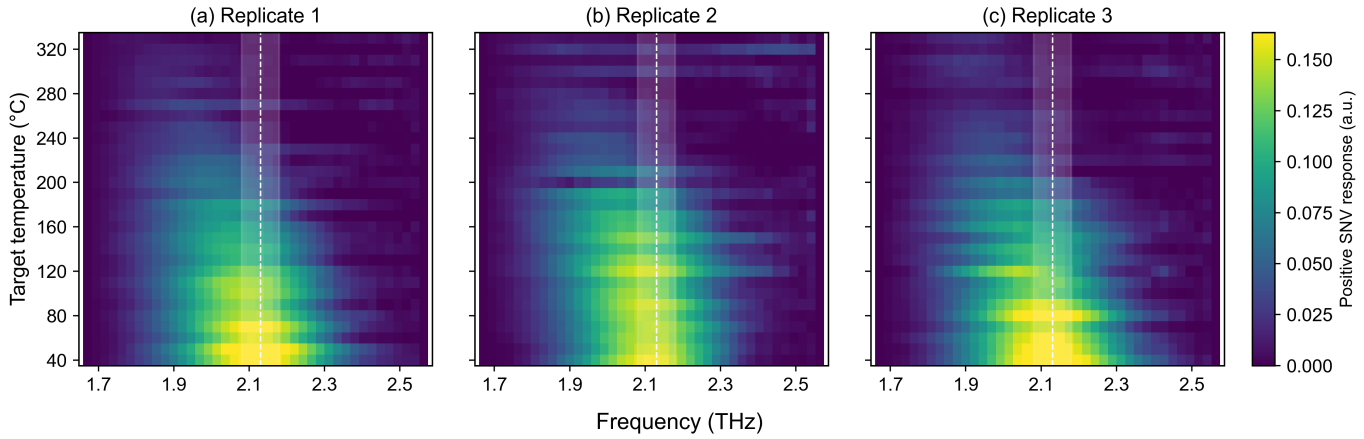


Figure 3. Frequency–temperature maps of the endpoint THz spectral response from three independent measurement sets. Panels (**a**–**c**) correspond to Replicates 1 to 3, respectively. Each horizontal row represents an endpoint spectrum obtained by averaging the final six time-resolved spectra at the corresponding target temperature. Color indicates the positive baseline-corrected SNV response, with warmer colors representing a stronger standardized spectral feature and cooler colors representing a weaker response. All panels use the same color scale, determined from the pooled values of the three measurement sets. Because the spectra were SNV-normalized, the displayed values represent relative spectral prominence rather than absolute absorption coefficients. The dashed line marks 2.13 THz, and the shaded region indicates the 2.13 ± 0.05 THz window used for the fixed-window response analysis.

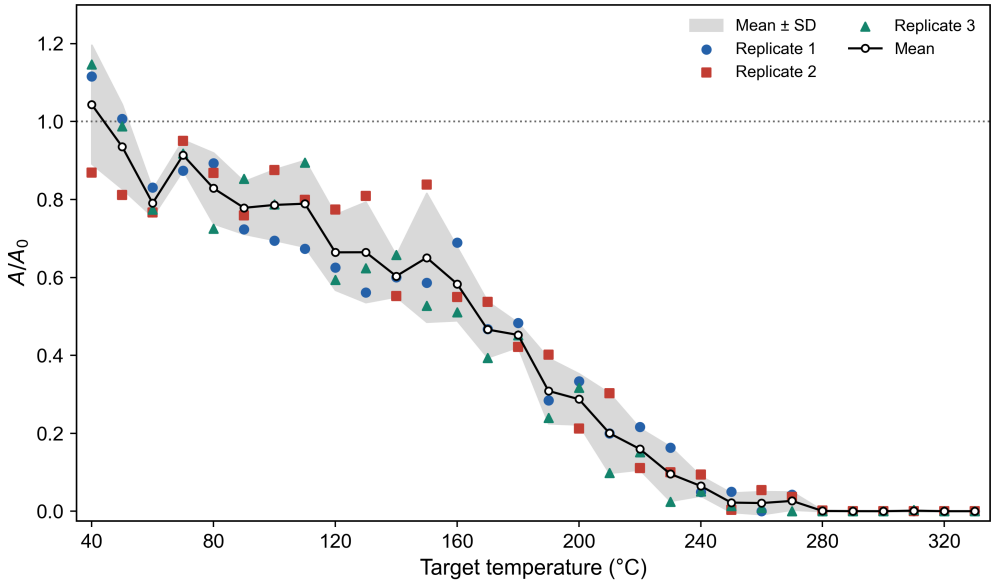


Figure 4. Endpoint response within the 2.13 ± 0.05 THz window as a function of target temperature. Colored symbols show the A/A_0 values from the three independent measurement sets. The black line and open circles show the mean, and the gray band shows ± standard deviation (SD; n = 3). For each heating run, A_0 was calculated from the first spectrum, and A was calculated from the endpoint spectrum obtained by averaging the final six time-resolved spectra. The dotted horizontal line indicates $A/A_0 = 1$, corresponding to no net change from the initial response. Connecting lines are visual guides and do not represent kinetic fits.

The center-shift-only calculation predicted a mean decrease of 1.8% in the fitted peak component within 2.08–2.18 THz between the 40 and 100 °C endpoints (n = 3), compared with a 26.1% decrease when all fitted peak parameters were allowed to change. Applying

the measured frequency grid and endpoint baseline gave a similar shift-only estimate of 2.0%. In the two 100 °C runs with quantitative preheating and endpoint fits, shifting the endpoint integration nodes increased A/A_0 from 0.695 to 0.709 and from 0.788 to 0.812. Thus, attenuation remained after allowing for the measurable peak displacement. This assessment applies to the range with identifiable peaks; at higher temperatures, the fixed-window signal is interpreted without assigning a peak position.

Despite fluctuations at individual temperatures, the three measurement sets followed a similar temperature-dependent decline. The mean A/A_0 decreased from 1.04 at 40 °C to 0.60 at 140 °C and 0.31 at 190 °C. It fell further to 0.096 at 230 °C and 0.022 at 250 °C, and remained close to zero from 280 °C onward. The decrease was not monotonic at every temperature interval, particularly between approximately 70 and 160 °C. The results therefore indicate a broad loss of endpoint response over the investigated temperature range rather than a sharply defined single-temperature transition. The time-resolved evolution underlying these endpoint values is examined in Section 3.2.

3.2. Phenomenological Analysis of Attenuation near 2.1 THz

To determine how the endpoint differences shown in Figure 4 developed during each heating run, the same fixed-window response ratio A/A_0 was examined as a function of time. Whereas the endpoint analysis used the mean response of the final six spectra, the present analysis retains the grouped time-resolved values throughout each run. It therefore provides phenomenological information about the apparent onset and progression of attenuation under the applied heating protocol.

Representative time-dependent profiles are shown in Figure 5. At lower target temperatures, the fixed-window response was largely retained, and A/A_0 remained close to unity or decreased only slightly during the measurement. At intermediate temperatures, the response decreased more clearly before approaching a residual level. At higher target temperatures, particularly at 210 °C and above, A/A_0 decreased rapidly and reached a substantially lower residual value. Despite fluctuations and differences in normalized response among the three measurement sets, the transition from weak attenuation at lower temperatures to rapid and extensive attenuation at higher temperatures was reproducible.

The mean fitted residual response, Y_{min}, decreased from 0.442 at 180 °C to 0.219 at 210 °C, marking a pronounced change in attenuation within this temperature range. Because $t = 0$ was defined before heating, the decrease observed during the first minute includes the temperature ramp and does not represent a one-minute isothermal transformation.

To relate the time-dependent attenuation profiles in Figure 5 to the applied heating program, the grouped A/A_0 values and their corresponding Equation (3) fits were remapped from elapsed time to estimated plate temperature using Equations (4) and (5). After the estimated plate temperature reached the set point, it was held at the target value in the mapping. Consequently, successive measurements acquired during the holding period share the same x coordinate. Only fits meeting the stated quality and physical-consistency criteria are displayed. This temperature-aligned representation was used to identify where attenuation occurred within the applied protocol.

Figure 6 separates the attenuation observed during the temperature ramp from that occurring after the estimated plate temperature reached the set point. None of the fits at 40 or 120 °C met the reliability criteria, although the experimental observations are retained in the figure. At 180 °C, reliable midpoints were obtained for two measurement sets, and both occurred after the estimated plate temperature had reached 180 °C. The fit for the third measurement set did not meet the R^2 criterion and is therefore shown without a fitted line or midpoint marker.

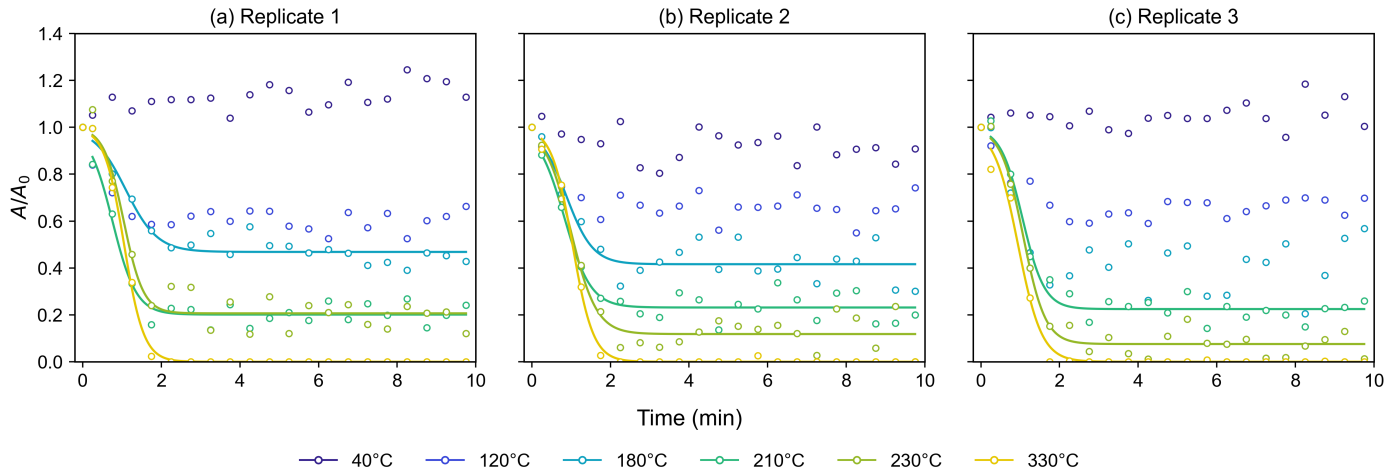


Figure 5. Time-dependent fixed-window response ratio A/A_0 at six representative target temperatures for (**a**) Replicate 1, (**b**) Replicate 2, and (**c**) Replicate 3. Open circles show all 30 s grouped observations, whereas solid curves show the logistic fits obtained using Equation (3) only when all reliability criteria defined in Section 2.4 were satisfied. Colors denote the target temperatures. The initial point at $t = 0$ and $A/A_0 = 1$ is shown for reference and was not included in the fitting.

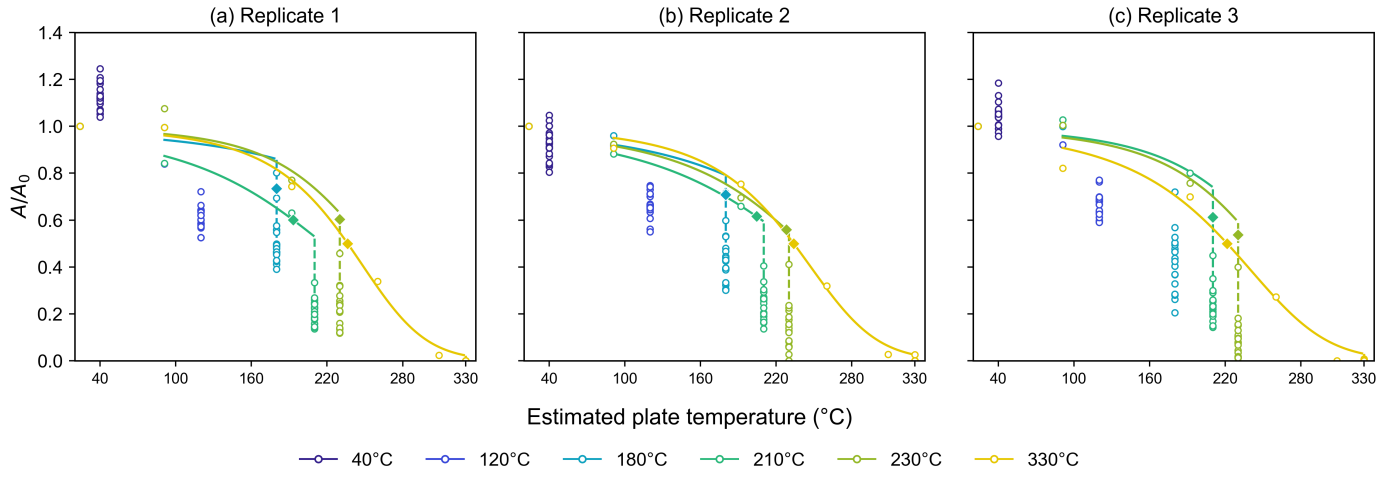


Figure 6. Temperature-aligned fixed-window response near 2.1 THz for three independent measurement sets (**a**–**c**). Colors denote target plate temperatures. Open circles show 30 s grouped A/A_0 observations; solid and dashed curves show reliable logistic-fit segments during the temperature ramp and subsequent holding period, respectively. Filled diamonds mark fitted midpoints. Elapsed time was converted to estimated plate temperature using Equations (4) and (5), and only fits meeting the criteria in Section 2.4 are shown.

For the 210 °C experiments, the reliable fitted midpoints corresponded to estimated plate temperatures of approximately 193, 204, and 210 °C. The corresponding values were approximately 228 to 230 °C for the 230 °C experiments. In the 330 °C experiments, all three midpoints occurred during the temperature ramp, at estimated plate temperatures of approximately 222 to 236 °C. Across the 210–330 °C experiments, the reliable midpoints therefore clustered at estimated plate temperatures of approximately 193–236 °C, defining the principal attenuation window under the applied protocol.

Several fitted midpoints occurred during the temperature ramp, whereas others occurred during the subsequent holding period. The THz response also continued to change after the estimated plate temperature reached the set point. The nonmonotonic $t_{1/2}$ and k values are therefore consistent with the combined influence of the temperature ramp and

exposure time, and are treated here as descriptors of the applied heating protocol rather than intrinsic kinetic constants.

This range overlaps the broad, moisture- and method-dependent region in which mobility-related transitions, water loss, and dehydration have been reported for cellulose [14,15]. Bulk liquid water produces strong broadband THz absorption across this frequency range rather than an isolated 2.13 THz line [28], while humidity-controlled measurements show that bound water shifts the cellulose-associated dielectric-loss feature near 2.13 THz [29]. Because the calibration represents the heating plate rather than the tablet, thermal contact resistance and temperature lag may shift the corresponding tablet temperature. Whether the pronounced heating-state attenuation persisted after cooling was tested directly by post-cooling THz-TDS and is examined together with the post-cooling XRD results in Section 3.3.

3.3. Post-Cooling Persistence of the THz Response and XRD Profile Stability

The pronounced attenuation described in Sections 3.1 and 3.2 was observed while the tablets remained under the applied heating protocol and therefore did not establish whether the temperature-dependent loss persisted after cooling. To address this question directly, tablets treated at eight selected target temperatures were remeasured by THz-TDS after cooling and dry equilibration.

As shown in Figure 7, a broad band near 2.1 THz remained detectable after cooling at every selected treatment temperature in all three measurement sets. The displayed peak height and detailed band shape varied among temperatures and measurement sets, but the post-cooling spectra did not show the progressive disappearance observed in the heating-endpoint spectra. The independently SNV-processed panels establish the continued visibility and approximate shape of the band, while the non-SNV R_{int} analysis below provides the quantitative comparison of temperature-dependent trends.

For the heating-endpoint series, the mean R_{int} decreased from 1.000 at 40 °C to 0.535 at 180 °C, 0.299 at 210 °C, and 0.091 at 230 °C. At 270 and 330 °C, the mean signed values were −0.070 and −0.183, respectively. Across the 15 linear-baseline placements, the corresponding means ranged from −0.099 to +0.041 and from −0.241 to −0.084. The 270 °C mean crossed zero, whereas the 330 °C mean remained negative throughout the tested placements. These signed values describe the net residual relative to the fitted linear background. The pronounced heating-endpoint decline was retained under every setting, while the sign at 270 °C and the magnitude of the negative values depended on baseline placement. In contrast, the mean post-cooling R_{int} values ranged from 0.887 to 1.093 across the selected treatment temperatures and showed no monotonic decline with increasing treatment temperature.

Because the heating-endpoint and post-cooling series were normalized separately to their corresponding 40 °C values, R_{int} compares the temperature dependence within each state rather than the absolute fraction recovered between sessions. The marked decline at the heating endpoint was absent from the post-cooling series.

The post-cooling XRD measurements then placed the THz and diffraction observations in the same nominal thermal state. The retained diffraction profiles were evaluated across the treatment-temperature series for changes in the cellulose I_β reflections, peak width, and fitted crystalline and amorphous contributions.

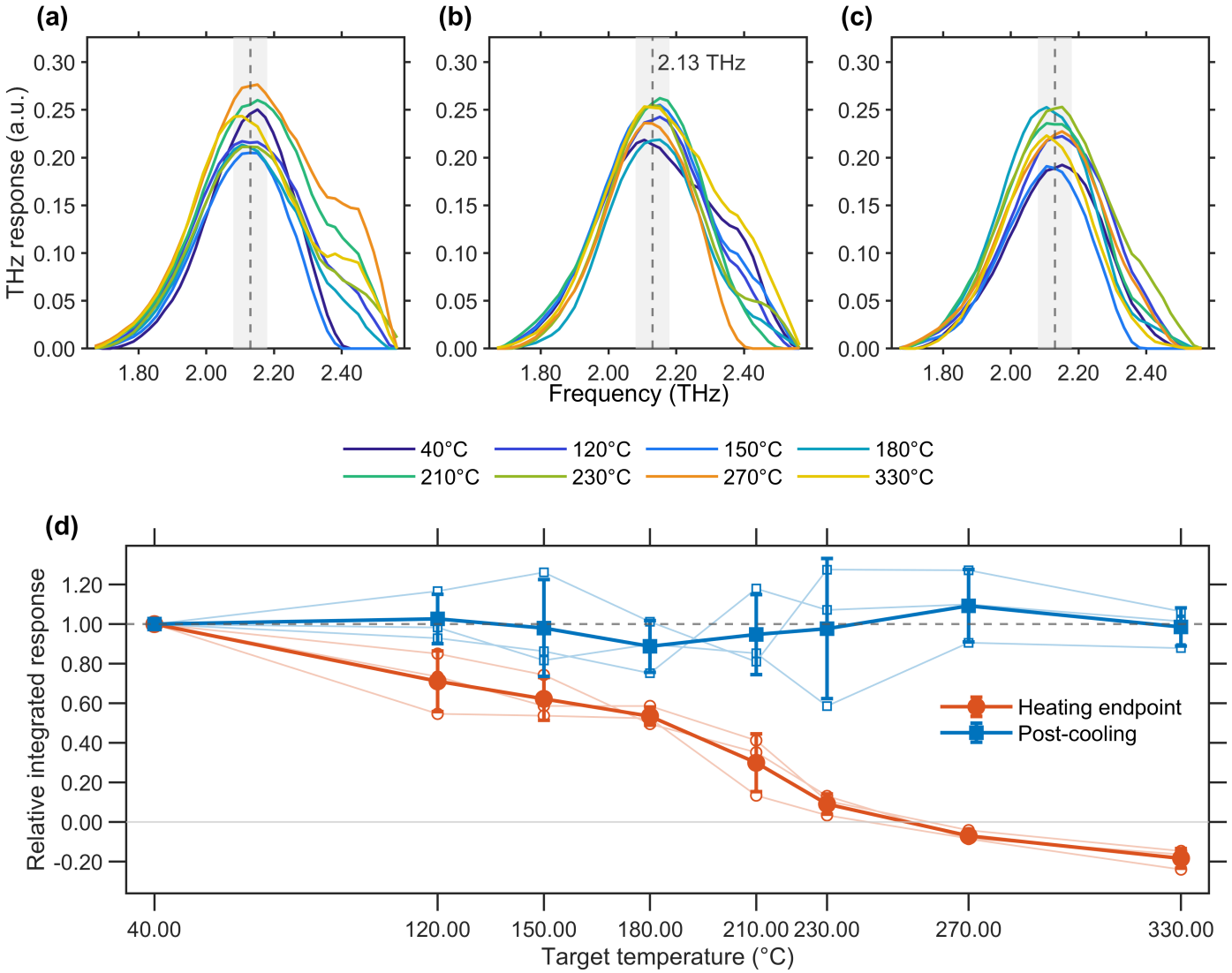


Figure 7. Post-cooling THz spectra and relative integrated-response trends. (**a**–**c**) SNV-processed spectra from three independent measurement sets. Solid colored curves represent post-cooling spectra at the target treatment temperatures indicated in the legend. The grey vertical dashed line and shaded region mark 2.13 THz and 2.13 ± 0.05 THz, respectively; these panels compare band visibility and shape. (**d**) Signed non-SNV R_{int} values at the heating endpoint and after cooling, normalized separately to the corresponding 40 °C value within each measurement state. Orange circles denote heating-endpoint measurements, and blue squares denote post-cooling measurements. Pale lines and open symbols show individual measurement sets; thick lines and filled symbols show the mean ± sample SD (n = 3). The grey horizontal dashed line marks R_{int} = 1, and the grey horizontal solid line marks R_{int} = 0. Connecting lines are visual guides. Panel (**d**) therefore compares within-state temperature trends. Negative values indicate a net integrated response below the fitted linear baseline; their sensitivity to baseline placement is described in the text.

As shown in Figure 8, the principal cellulose I_β diffraction features present in the unheated reference were retained in the post-cooling patterns across the investigated target-temperature range. Relative peak intensities differed between the unheated reference and the treated tablets. Within the post-cooling series, no characteristic reflection showed a clear progressive disappearance, and no new reflection became evident as the target temperature increased. The principal features showed no consistently increasing broadening. The heatmap in Figure 8b likewise showed no clear monotonic evolution in the overall diffraction-profile shape from 40 to 330 °C.

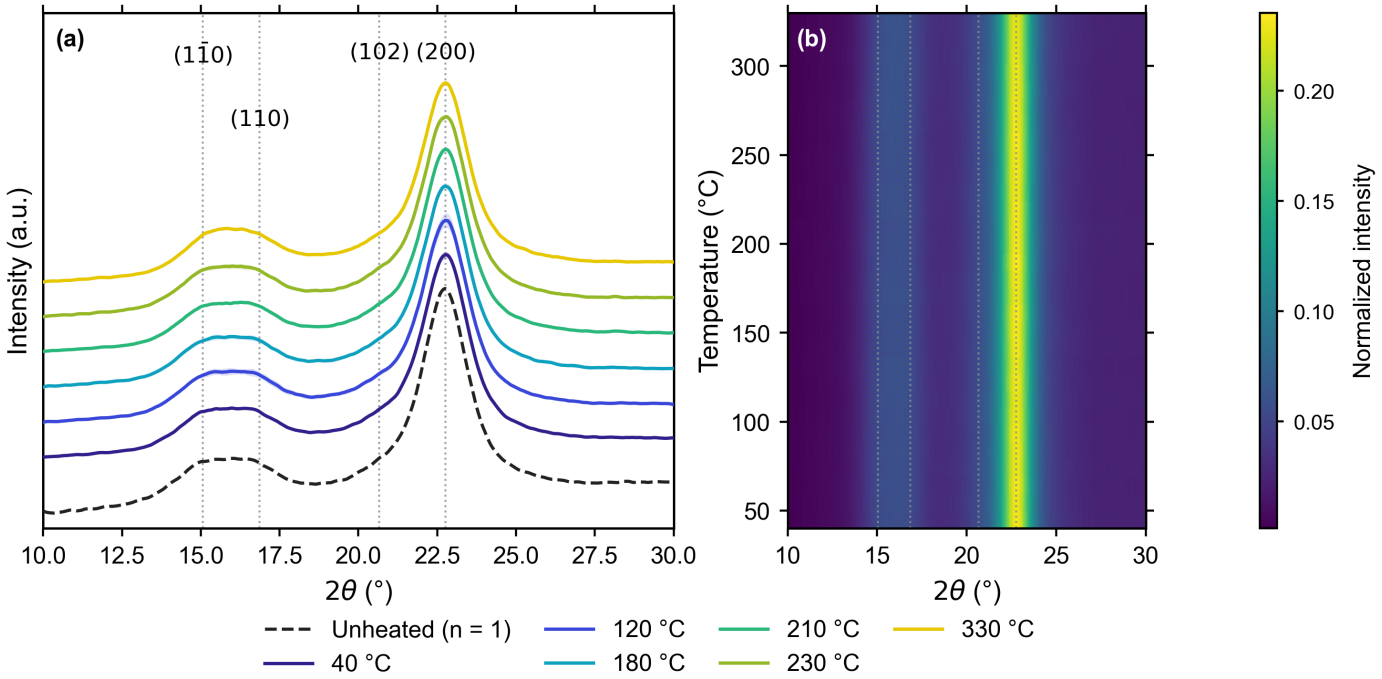


Figure 8. *X*-ray diffraction (XRD) profiles of unheated and thermally treated microcrystalline cellulose (MCC) tablets. (**a**) The dashed black curve shows one unheated tablet from the same preparation batch. Colored curves show post-cooling mean profiles at target temperatures of 40, 120, 180, 210, 230, and 330 °C; shading indicates ± standard deviation (n = 3). All profiles were area-normalized within 2θ = 10–30°, rigidly aligned to the 40–90 °C reference for shape comparison, and vertically offset. Mild Savitzky–Golay smoothing was used only for display. Dotted lines mark the reference positions of the cellulose I_β $(1\bar{1}0)$, (110), (102), and (200) reflections. (**b**) Heatmap of the unsmoothed mean area-normalized and aligned post-cooling profiles over 40–330 °C.

The constrained model reproduced the principal features of the representative mean profiles at 40, 180, and 330 °C (Figure 9a–c), with fit R^2 values of 0.9935, 0.9943, and 0.9911, respectively. The corresponding root-mean-square residuals were 1.73%, 1.64%, and 2.02% of the observed intensity ranges. The residual strips show structured deviations in the low-angle peak region and near the interval edges. The dominant (200) contribution and the overlapping lower-angle features remained evident in all three representative profiles. Yao et al. [23] also reported imperfect fits at 2θ = 27–31° and suggested contributions from weak crystalline reflections omitted from their conventional peak model. They noted that adding these reflections would increase the complexity and uncertainty of the deconvolution. Unresolved weak reflections may likewise contribute to the high-angle residuals here, alongside background and peak-shape mismatch.

Under the original fitting model, the unheated reference gave an apparent crystalline-area fraction of 67.7%. The post-cooling temperature means ranged from 64.0 to 66.0%, approximately 1.7–3.8 percentage points below that single reference, and fluctuated without a progressive decline across the treatment series (Figure 9d). The fitted amorphous contribution varied correspondingly from approximately 34.0 to 36.0%. These values describe relative fitted component areas within 10–30°. With only one unheated profile, the unheated-to-treated difference is descriptive and does not establish a statistically resolved change in crystallinity.

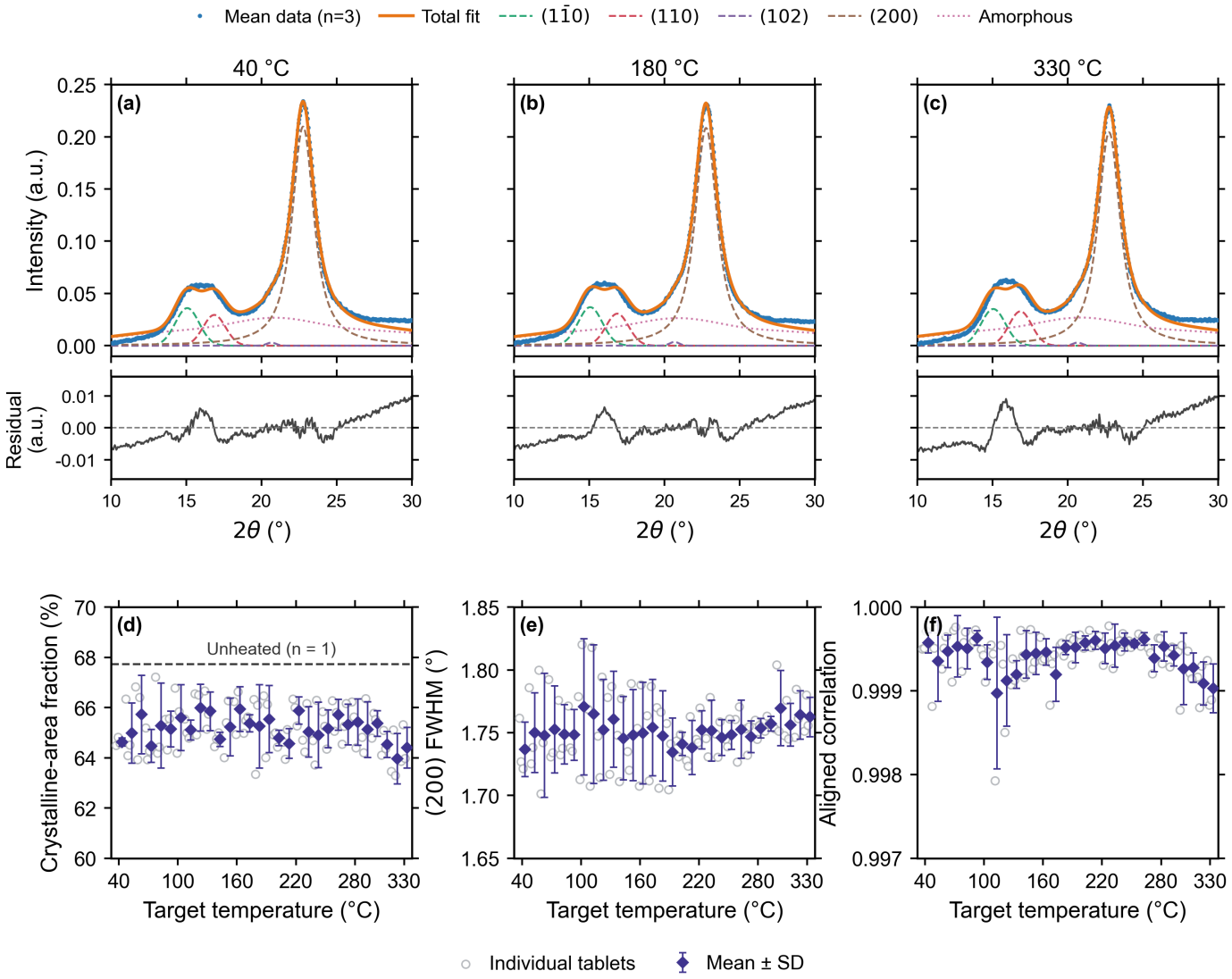


Figure 9. Constrained deconvolution and quantitative XRD descriptors after cooling. (**a**–**c**) Area-normalized mean profiles (n = 3) and constrained fits after treatment at 40, 180, and 330 °C. Component curves show the cellulose I_β reflections and amorphous contribution; the lower strip of each panel shows the unsmoothed residual (observed minus fitted intensity), with a dashed zero line. (**d**–**f**) Apparent crystalline-area fraction, constrained (200) FWHM, and whole-pattern correlation with the 40–90 °C reference, respectively. Gray circles show individual tablets; purple diamonds and error bars show mean ± sample SD (n = 3). The dashed line in (**d**) marks the single unheated reference (67.7%). Fractions and widths were fitted to individual background-corrected patterns without prior normalization or alignment; correlations used aligned, area-normalized profiles. Horizontal offsets are used only for clarity.

The nine Fourier-profile settings gave post-cooling temperature means spanning 59.3–69.0%, with a maximum offset of 4.7 percentage points from the original model at the same temperature. Within any one setting, the range across temperatures was 1.9–2.3 percentage points. The separate Gaussian shape check gave 60.6–62.9%. The tested Fourier-profile changes preserved the relatively small temperature span within the original constrained framework. The division of the observed intensity into components also depends on the crystalline peak shapes and background description. The area fractions therefore provide model-dependent descriptors of the cooled specimens.

The mean constrained FWHM of the (200) component ranged from 1.735° to 1.771° (Figure 9e). Although differences occurred between individual temperatures and tablets, the FWHM did not show consistently increasing broadening with target temperature. The mean aligned whole-pattern correlation remained between 0.99897 and 0.99963 (Figure 9f), indicating that the post-cooling profile shapes remained highly similar to the low-temperature reference after correction for rigid specimen-position shifts. Within the adopted analysis, the temperature-to-temperature fluctuations overlapped substantially with the variation among the independently prepared tablets and did not define a common monotonic temperature dependence across the three descriptors.

Taken together, the post-cooling measurements show that the temperature-ordered attenuation observed during heating was no longer present after cooling. The 2.1 THz band remained detectable, and the post-cooling R_{int} values fluctuated around their respective 40 °C references without a systematic decline. The XRD patterns retained the principal cellulose I_β reflections. This comparison supports the persistence of the main diffraction features after cooling, while quantitative changes in crystalline content remain sensitive to the deconvolution model.

The possible origins of the heated-state attenuation and the post-cooling band are discussed together with the color results in Section 3.5.

3.4. Image-Based Tablet Color Analysis

Post-treatment color was examined alongside the THz responses measured during heating and after cooling. Figure 10a compares representative scans of the actual tablets with color swatches reconstructed from the mean CIELAB coordinates at the same target temperatures. The scans retain the visible surface variation, while the swatches summarize the mean color across the three measurement sets. The tablets remained nearly white from 40 to 150 °C, showed a pale yellow color at approximately 180 °C, and became progressively yellowish brown from 210 to 330 °C.

The image-derived CIELAB parameters provide comparative measures of this color evolution (Figure 10b–d). The L^* value remained close to its initial level through the lower-temperature region and began to decrease above approximately 170–180 °C, with a larger reduction at higher temperatures (Figure 10b). This decrease corresponds to progressive darkening of the tablets. The a^* value remained close to zero at lower temperatures, decreased slightly between approximately 160 and 190 °C, and subsequently increased markedly above approximately 200 °C (Figure 10c). The high-temperature increase in a^* indicates the development of a stronger red component. The b^* value remained low up to approximately 150 °C and then increased from approximately 160 °C onward (Figure 10d). Because b^* began to increase while L^* was still comparatively high, yellowing became detectable before the strongest darkening occurred.

The overall color difference, ΔE^*_{ab}, was calculated relative to the fixed unheated-tablet reference, as shown in Figure 10e. It remained generally small through the lower-temperature region and increased progressively from approximately 160 °C onward. The increase became more pronounced above 200 °C and reached its largest values at the highest target temperatures. This trend agrees with the transition from pale yellow to yellowish brown in Figure 10a and shows that substantial visible alteration developed mainly in the intermediate- and high-temperature regions.

Comparison of the heating-endpoint THz response with the post-treatment color parameters showed different dependencies on target temperature. The fixed-window THz response had already decreased substantially at intermediate target temperatures, whereas the overall color difference remained comparatively small through approximately 150 °C. Yellowing became more evident from approximately 160 °C, followed by pronounced increases

in redness, yellowness, and darkening above approximately 200 °C. The heated-state THz attenuation therefore became evident at lower target temperatures than pronounced post-treatment discoloration. This comparison concerns their different treatment-temperature dependencies rather than a within-run temporal sequence.

The retained color changes followed a different pattern from the post-cooling THz and XRD responses. Discoloration increased progressively, whereas the 2.1 THz band remained detectable and neither R_{int} nor the XRD descriptors showed a corresponding monotonic decline. Persistent discoloration is compatible with chromophore formation or other chemical changes during thermal treatment [16]. The image-derived color data alone cannot identify the responsible reactions or products. These observations show that lasting visible alteration can coexist with a detectable cellulose-related THz band and retained principal diffraction features.

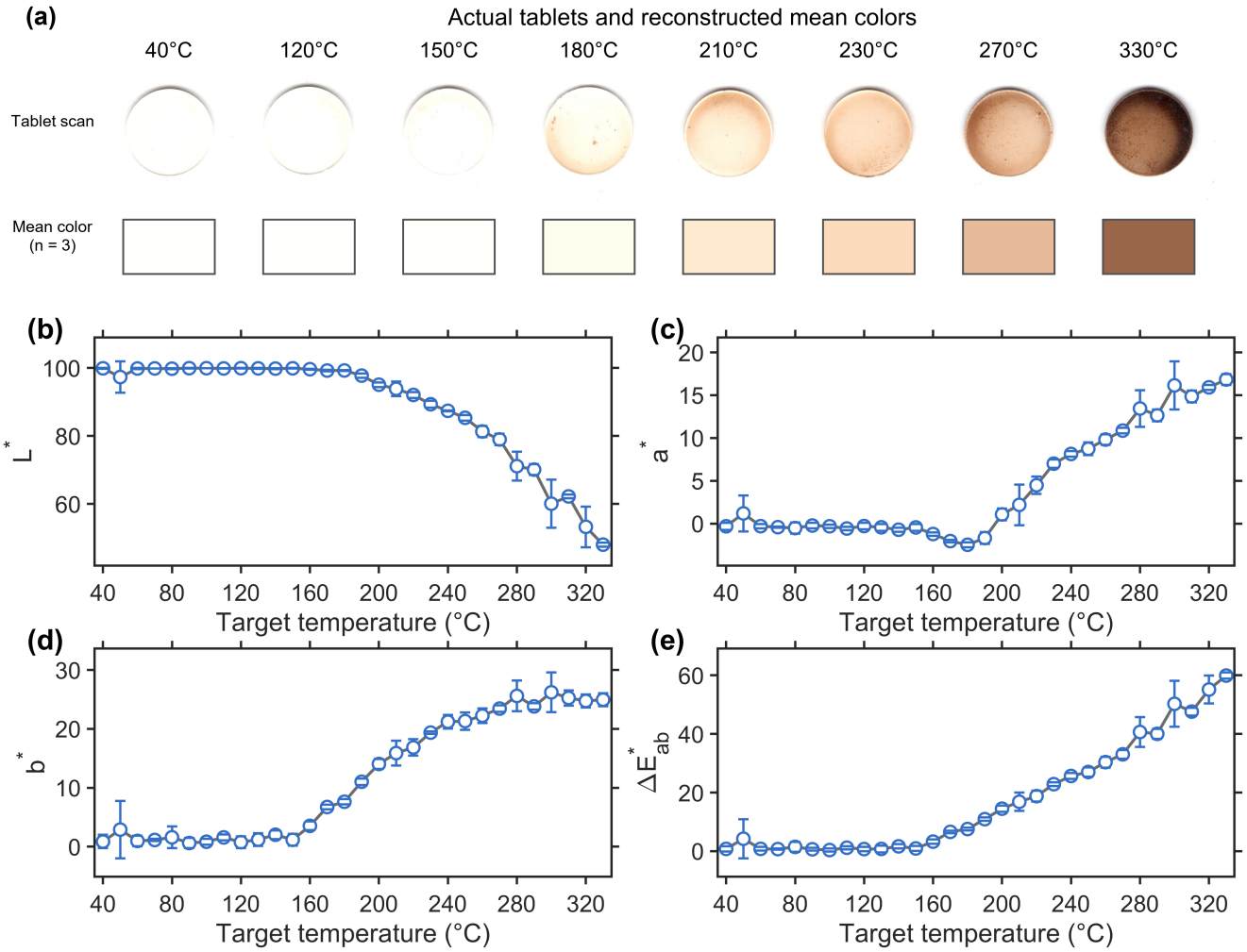


Figure 10. Image-based color analysis of MCC tablets after thermal treatment. (**a**) Representative actual tablet scans (**upper row**) and color swatches reconstructed from the mean CIELAB coordinates of all three sets (**lower row**) at the same target temperatures. The 40 °C scan is from measurement set 3, the 120 °C scan is from measurement set 2, and the remaining scans are from measurement set 1. The scans show complete tablets at a common scale, with their original colors retained. Temperature-dependent changes in (**b**) L^*, (**c**) a^*, (**d**) b^*, and (**e**) ΔE^*_{ab}. Data are mean ± standard deviation for three independently prepared tablets at each temperature (n = 3). ΔE^*_{ab} was calculated in the International Commission on Illumination (CIE) 1976 $L^*a^*b^*$ (CIELAB) color space relative to the fixed unheated-tablet reference. Color values are comparative image-derived measurements obtained without calibration against a color standard.

3.5. Mechanistic Interpretation and Outlook

We propose that heating alters the interchain environment supporting the cellulose-associated collective vibration near 2.1 THz, reducing its spectral prominence. Changes in hydrogen-bond organization, molecular mobility, and hydration are plausible contributors [20,29]. The peak-displacement analysis shows that the measurable shift accounts for only a small part of the attenuation over 40–100 °C, while the pronounced heating-endpoint decline persists across the tested baseline placements. These findings support a change in the resolved vibrational response, although they do not establish the molecular pathway responsible for it.

After cooling, the band is again detectable alongside the principal cellulose I_β diffraction features. Ordered regions may remain through treatment, and structural reorganization during cooling may also contribute to the observed response. Persistent discoloration at higher setpoints suggests that lasting chemical alteration could coexist with these retained spectral and diffraction features. A reversible contribution to the spectral response may also be present. The relative contributions of thermal-state effects, chemical alteration, and cooling-induced reorganization remain to be established.

Temperature-resolved XRD during heating, holding, and cooling would be a valuable next step. Measurements under thermal programs and atmospheric conditions matched to the THz experiments, with sample temperature monitored, could track the principal reflection positions, widths, and intensities through the attenuation interval. This would help establish whether changes in Bragg-coherent order accompany the weakening of the THz band and how the diffraction features evolve during cooling. Complementary measurements under controlled hydration, together with mass-loss and chemical characterization, would help assess the contributions of water and persistent chemical alteration.

3.6. Implications for Thermal-Treatment Monitoring and Material Assessment

The present findings support using the 2.1 THz response to follow changes in cellulose during thermal treatment. Its pronounced attenuation during heating and subsequent detection after cooling show that measurements of the cooled material can miss a substantial part of the spectral response during processing. This adds a temporal perspective to earlier work that related the post-treatment 3.04 THz band to XRD-derived crystallinity [22]. Here, the attenuation profiles locate changes within the heating program, including changes during the temperature ramp before the target temperature is reached (Section 3.2). Such information could help compare heating programs and select intervals for closer examination or product sampling. The difference between the heated and cooled spectra also matters when developing THz-based process indicators: a weak band during heating alone does not establish a lasting loss of cellulose order. Calibration against the properties of the treated material should therefore account for the temperature and timing of the spectral measurement.

For assessment after treatment, the coexistence of persistent discoloration, a detectable 2.1 THz band, and retained principal diffraction features shows why appearance and structural measurements provide complementary criteria. Earlier color-kinetic work established color as a record of thermal exposure [16]. Our comparison with THz-TDS and XRD shows that substantial visible alteration can remain even when the cooled spectra and diffraction profiles retain their main cellulose features. Assessment based only on band visibility could consequently overlook changes relevant to appearance-sensitive uses. Pairing the heating profiles with post-cooling color and structural measurements could help screen treatment conditions when both appearance and cellulose organization matter. Relationships with properties such as strength or dimensional stability would then determine which combinations of these observations are useful for a particular material.

The time-dependent response also suggests a possible contribution to studies of cellulose conversion. In hydrothermal carbon-sphere synthesis, independently varied temperature and pressure were related to the composition and structure of recovered products [30]. A complementary question is how the cellulose vibrational response evolves before those products are recovered. The present measurements identify a response that can be followed during dry heating and show why its trajectory can contain information absent after cooling. Applied to conversion studies, this approach could guide sampling around spectral changes and test their relationship to product formation. Extension to aqueous reactors would require suitable optical access and control of water absorption [28], followed by calibration against conversion and product properties. Table 1 summarizes these links between earlier evidence, the information added by the present findings, and possible uses.

Table 1. Possible applications of the present findings and the information they add to related studies.

Application	Earlier Evidence and Open Question	Information Added by This Study	Possible Use of the Findings
Monitoring thermal treatment	Post-treatment THz-TDS and XRD describe changes associated with heating conditions [22]. The spectral trajectory during heating is not captured by these endpoint measurements.	The 2.1 THz profiles locate attenuation during the ramp and holding stages. Band detection after cooling shows that the heated and cooled measurements can give different pictures.	Compare heating programs and identify intervals for closer examination; account for measurement state when calibrating spectral process indicators.
Assessing treated cellulosic materials	Color kinetics describe accumulated visible change [16]; post-treatment THz-TDS and XRD characterize retained structural features [22]. Their relation to the response during heating needs to be established.	Persistent discoloration coexists with the post-cooling band and principal diffraction features, despite pronounced attenuation during heating. Appearance and spectral persistence therefore provide different information.	Screen treatments using heating profiles together with post-cooling color and structural criteria; relate these observations to the properties required for the intended use.
Developing cellulose-conversion diagnostics	Hydrothermal treatment links temperature and pressure to recovered carbon products [30]. The cellulose vibrational response during conversion remains a complementary question.	Dry-MCC measurements identify a time-dependent spectral observable and demonstrate the value of comparing measurements during heating and after cooling.	Explore spectral changes as a guide for product sampling and conversion studies, with optical adaptation and calibration for aqueous conditions.

MCC: microcrystalline cellulose; THz-TDS: terahertz time-domain spectroscopy; XRD: X-ray diffraction.

4. Conclusions

THz-TDS captured the attenuation of the cellulose I-related band near 2.1 THz during a 10 min heating protocol. For experiments at target temperatures of 210–330 °C, reliable attenuation midpoints occurred at estimated plate temperatures of approximately 193–236 °C. At high target temperatures, the band became unidentifiable, while the reference-only heating control showed only minor variation near 2.1 THz. After cooling, the band was detectable at every selected treatment temperature, and the independently normalized R_{int} values showed no corresponding monotonic decline. The principal cellulose I_β reflections were retained after cooling; the fitted crystalline-area fractions describe the cooled specimens within the adopted deconvolution model. Pronounced discoloration persisted mainly above approximately 200 °C, showing that lasting visible alteration can coexist with the post-cooling spectral and diffraction features. These observations demonstrate the value of

following the vibrational response during heating alongside measurements of the cooled material. Time-resolved THz measurements could help compare heating programs, with post-cooling spectra, diffraction, and color measurements providing complementary criteria for assessing the treated material. Relating these observations to final material properties would support their use in selecting thermal-treatment conditions.

Author Contributions: L.C.: Conceptualization, Data Curation, Formal Analysis, Methodology, Writing—Original Draft, Writing—Review & Editing. T.I.: Investigation, Funding Acquisition, Methodology, Writing—Review & Editing. T.M.: Writing—Review & Editing. S.T.: Writing—Review & Editing. H.W.: Investigation, Methodology, Writing—Review & Editing. All authors have read and agreed to the published version of the manuscript.

Funding: This research was funded by the Japan Society for the Promotion of Science (JSPS) through KAKENHI (Grant Numbers JP21H02255, JP23K19305, and JP26K18104) and by the Japan Science and Technology Agency (JST) through its Fusion Oriented REsearch for disruptive Science and Technology (FOREST) Program (Grant Number JPMJFR243E).

Institutional Review Board Statement: Not applicable.

Data Availability Statement: The raw data supporting the conclusions of this article will be made available by the authors on request.

Conflicts of Interest: The authors declare no conflicts of interest.

References

1. Nishiyama, Y.; Sugiyama, J.; Chanzy, H.; Langan, P. Crystal Structure and Hydrogen Bonding System in Cellulose I_α from Synchrotron X-ray and Neutron Fiber Diffraction. *J. Am. Chem. Soc.* **2003**, *125*, 14300–14306. [CrossRef] [PubMed]
2. Nishiyama, Y.; Langan, P.; Chanzy, H. Crystal Structure and Hydrogen-Bonding System in Cellulose Iβ from Synchrotron X-ray and Neutron Fiber Diffraction. *J. Am. Chem. Soc.* **2002**, *124*, 9074–9082. [CrossRef] [PubMed]
3. Park, S.; Baker, J.O.; Himmel, M.E.; Parilla, P.A.; Johnson, D.K. Cellulose crystallinity index: Measurement techniques and their impact on interpreting cellulase performance. *Biotechnol. Biofuels* **2010**, *3*, 10. [CrossRef] [PubMed]
4. French, A.D. Idealized powder diffraction patterns for cellulose polymorphs. *Cellulose* **2014**, *21*, 885–896. [CrossRef]
5. Himmel, M.E.; Ding, S.Y.; Johnson, D.K.; Adney, W.S.; Nimlos, M.R.; Brady, J.W.; Foust, T.D. Biomass Recalcitrance: Engineering Plants and Enzymes for Biofuels Production. *Science* **2007**, *315*, 804–807. [CrossRef] [PubMed]
6. Hall, M.; Bansal, P.; Lee, J.H.; Realff, M.J.; Bommarius, A.S. Cellulose crystallinity—A key predictor of the enzymatic hydrolysis rate. *FEBS J.* **2010**, *277*, 1571–1582. [CrossRef] [PubMed]
7. Esteves, B.; Pereira, H. Wood modification by heat treatment: A review. *BioResources* **2009**, *4*, 370–404. [CrossRef]
8. Poncsák, S.; Kocaefe, D.; Bouazara, M.; Pichette, A. Effect of high temperature treatment on the mechanical properties of birch (*Betula papyrifera*). *Wood Sci. Technol.* **2006**, *40*, 647–663. [CrossRef]
9. Kocaefe, D.; Poncsak, S.; Tang, J.; Bouazara, M. Effect of heat treatment on the mechanical properties of North American jack pine: Thermogravimetric study. *J. Mater. Sci.* **2010**, *45*, 681–687. [CrossRef]
10. García-Iruela, A.; Esteban, L.G.; García Fernández, F.; de Palacios, P.; Rodriguez-Navarro, A.B.; Martín-Sampedro, R.; Eugenio, M.E. Changes in cell wall components and hygroscopic properties of Pinus radiata caused by heat treatment. *Eur. J. Wood Wood Prod.* **2021**, *79*, 851–861. [CrossRef]
11. Bhuiyan, M.T.R.; Hirai, N.; Sobue, N. Changes of crystallinity in wood cellulose by heat treatment under dried and moist conditions. *J. Wood Sci.* **2000**, *46*, 431–436. [CrossRef]
12. Bhuiyan, T.R.; Hirai, N. Study of crystalline behavior of heat-treated wood cellulose during treatments in water. *J. Wood Sci.* **2005**, *51*, 42–47. [CrossRef]
13. Poletto, M.; Zattera, A.J.; Forte, M.M.C.; Santana, R.M.C. Thermal decomposition of wood: Influence of wood components and cellulose crystallite size. *Bioresour. Technol.* **2012**, *109*, 148–153. [CrossRef] [PubMed]
14. Picker, K.M.; Hoag, S.W. Characterization of the thermal properties of microcrystalline cellulose by modulated temperature differential scanning calorimetry. *J. Pharm. Sci.* **2002**, *91*, 342–349. [CrossRef] [PubMed]
15. Nam, S.; Hillyer, M.B.; Condon, B.D. Method for identifying the triple transition (glass transition-dehydration-crystallization) of amorphous cellulose in cotton. *Carbohydr. Polym.* **2020**, *228*, 115374. [CrossRef] [PubMed]

16. Matsuo, M.; Umemura, K.; Kawai, S. Kinetic analysis of color changes in cellulose during heat treatment. *J. Wood Sci.* **2012**, *58*, 113–119. [CrossRef]
17. Vieira, F.S.; Pasquini, C. Determination of Cellulose Crystallinity by Terahertz-Time Domain Spectroscopy. *Anal. Chem.* **2014**, *86*, 3780–3786. [CrossRef] [PubMed]
18. Wang, H.; Horikawa, Y.; Tsuchikawa, S.; Inagaki, T. Terahertz time-domain spectroscopy as a novel tool for crystallographic analysis in cellulose. *Cellulose* **2020**, *27*, 9767–9777. [CrossRef]
19. Wang, H.; Kataoka, H.; Tsuchikawa, S.; Inagaki, T. Terahertz time-domain spectroscopy as a novel tool for crystallographic analysis in cellulose: Cellulose I to cellulose II, tracing the structural changes under chemical treatment. *Cellulose* **2022**, *29*, 3143–3151. [CrossRef]
20. Verhaeg, E.A.; Hoshina, H.; Kikuchi, J.; Catalano, L.; Ruggiero, M.T. Solving the cellulose I polymorphic structural riddle: Disorder in hydrogen bond networks activates diagnostic terahertz dynamics. *J. Mater. Chem. C* **2025**, *13*, 15328–15337. [CrossRef]
21. Wang, H.; Tsuchikawa, S.; Inagaki, T. Terahertz time-domain spectroscopy as a novel tool for crystallographic analysis in cellulose: The potentiality of being a new standard for evaluating crystallinity. *Cellulose* **2021**, *28*, 5293–5304. [CrossRef]
22. Wang, H.; Asaoka, M.; Tsuchikawa, S.; Inagaki, T. Investigation of crystallinity changes in thermally-treated wood using THz time-domain spectroscopy. *Cellulose* **2026**, *33*, 681–693. [CrossRef]
23. Yao, W.; Weng, Y.; Catchmark, J.M. Improved cellulose X-ray diffraction analysis using Fourier series modeling. *Cellulose* **2020**, *27*, 5563–5579. [CrossRef]
24. Thompson, P.; Cox, D.E.; Hastings, J.B. Rietveld refinement of Debye–Scherrer synchrotron X-ray data from Al_2O_3. *J. Appl. Crystallogr.* **1987**, *20*, 79–83. [CrossRef]
25. Richards, F.J. A Flexible Growth Function for Empirical Use. *J. Exp. Bot.* **1959**, *10*, 290–301. [CrossRef]
26. *ISO/CIE 11664-4:2019*; Colorimetry—Part 4: CIE 1976 $L^*a^*b^*$ Colour Space. International Organization for Standardization: Geneva, Switzerland, 2019.
27. Foltynowicz, R.J.; Allman, R.E. *Terahertz Time-Domain Spectroscopy of Atmospheric Water Vapor from 0.4 to 2.7 THz*; Technical Report SAND2005-5709, 876363; Sandia National Laboratories: Albuquerque, NM, USA , 2005. [CrossRef] [PubMed]
28. Xu, J.; Plaxco, K.W.; Allen, S.J. Absorption spectra of liquid water and aqueous buffers between 0.3 and 3.72 THz. *J. Chem. Phys.* **2006**, *124*, 036101. [CrossRef] [PubMed]
29. Wang, H.; Yamamoto, H.; Yoshida, M.; Tsuchikawa, S.; Inagaki, T. Terahertz time-domain spectroscopy as a novel tool for crystallographic analysis in cellulose: Insights into the complex lattice interaction with water molecules. *Cellulose* **2026**, *33*, 7665–7676. [CrossRef]
30. Yu, S.; Dong, X.; Zhao, P.; Luo, Z.; Sun, Z.; Yang, X.; Li, Q.; Wang, L.; Zhang, Y.; Zhou, H. Decoupled temperature and pressure hydrothermal synthesis of carbon sub-micron spheres from cellulose. *Nat. Commun.* **2022**, *13*, 3616. [CrossRef] [PubMed]

Disclaimer/Publisher's Note: The statements, opinions and data contained in all publications are solely those of the individual author(s) and contributor(s) and not of MDPI and/or the editor(s). MDPI and/or the editor(s) disclaim responsibility for any injury to people or property resulting from any ideas, methods, instructions or products referred to in the content.